Journal of Applied Fluid Mechanics, Vol. 18, No. 9, pp. 2361-2376, 2025.
Available online at www.jafmonline.net, ISSN 1735-3572, EISSN 1735-3645.
https://doi.org/10.47176/jafm.18.9.3300

Investigation of a Vacuum Ejector Used in a Dynamic Function Vehicle Tire Air Control Valve

Y. S. Korkmaz[1,2†], A. Kibar[3], K. Suleyman Yigit[4], E. Erturk[5] and Z. Doğruyol[1]

[1] *Altan Hydraulic Engineering Industry and Trade Corporation, Istanbul, 34956, Turkey*
[2] *Department of Mechanical Engineering, Graduate School of Natural and Applied Sciences, Kocaeli University, Umuttepe Campus, 41380, Kocaeli, Turkey*
[3] *Department of Mechanical and Material Technologies, Kocaeli University, Uzunciftlik Nuh Cimento Campus, 41180, Kocaeli, Turkey*
[4] *Department of Mechanical Engineering, Faculty of Engineering, Kocaeli University, Umuttepe Campus, 41380, Kocaeli, Turkey*
[5] *Department of Mechanical Engineering, Medeniyet University, North Campus, 34700, Istanbul, Turkey*

†*Corresponding Author Email: 206109014@kocaeli.edu.tr*

ABSTRACT

A critical component of a central tyre inflation system (CTIS) is the tyre valve. When positive pressure air is directed to the valve, it allows air to enter the tyre, increasing the tyre's internal pressure. Conversely, when vacuum pressure is applied, the tyre pressure decreases. Consequently, the tyre valve must be capable of generating negative pressure when necessary to function effectively. While the CTIS includes a compressed air reservoir and a pressure pump for reservoir filling, it lacks a dedicated vacuum pump to create negative pressure. Instead, negative pressure is generated by an ejector that utilises the Venturi effect to accelerate the air through an orifice, creating low pressure using pressurised air from the reservoir. The primary advantage of this design is its ability to generate negative pressure without an additional component, such as a vacuum pump, relying solely on the existing high-pressure air. This study presents both experimental and numerical investigations of a vacuum ejector designed to generate negative pressure. The experimental results align closely with the numerical simulations. Furthermore, the study explores the impact of varying the throat diameter of the vacuum ejector to enhance fluid velocity, with the optimal performance observed at −98 kPa for a 1 mm throat diameter. For throat diameters of <1 mm, the flow becomes unstable, and at 0.2 mm, the flow is completely obstructed, rendering the system inoperative.

Article History

Received December 14, 2024
Revised March 9, 2025
Accepted April 11, 2025
Available online July 5, 2025

Keywords:

Computational fluid dynamics
Central tyre inflation system
Pneumatic
Vacuum
Valve

1. INTRODUCTION

Vacuum technology, commonly employed in various industrial processes, utilises equipment such as vacuum generators, pumps, and ejectors (Macia et al., 2019). Vacuum ejectors are widely used in various industries, such as the oil and gas sector, refrigeration and air conditioning systems, and aerospace systems, to generate a vacuum. These ejectors typically consist of three sections: inlet, suction, and exhaust. A pressurised fluid is sent into the ejector through the inlet, where its velocity increases and pressure decreases, creating a vacuum. A secondary fluid is drawn into the suction section, and it mixes within the ejector before being expelled through the exhaust section.

Vacuum ejectors can be designed in various configurations depending on their application. Their advantages include simplicity, absence of moving parts, no need for electricity, and customisation for different flow rates and pressures. However, they have drawbacks, including low efficiency, limited suction capacity, noise, and high air consumption (Mukhtar et al., 2024; Sadeghiseraji et al., 2024).

One significant application of vacuum ejectors is in central tyre inflation systems (CTIS), in which vacuum ejectors, which are compact and cost-effective, facilitate the air expulsion process from the tyre valve. By creating a negative pressure in the tyre valve, these ejectors enable the release of pressurised air from the tyre. However, without careful design consideration, vacuum ejectors may operate with low efficiencies and fail to provide adequate vacuum. Factors such as diameter, length, and type of fluid can significantly affect the performance of vacuum ejectors. The effect of the ejector geometry may

be subtle under steady-state conditions but more significant under varying operational conditions (Kuo et al., 2023).

The vacuum creation process in ejectors typically accounts for 50–80% of the total operational time. During this process, maintaining a continuous supply of high-pressure air is essential to sustain the vacuum level. One way to reduce air consumption is with a small-diameter nozzle, although this may reduce the vacuum effect (Niu & Zhang, 2024). Moreover, vacuum ejectors are energy-intensive during operation, and long response times can further reduce efficiency while increasing air consumption. For optimal energy use, the feeding pressure should be minimised. Specifically, many vacuum ejectors generate a vacuum of −90 kPa when the feeding pressure reaches 550 kPa (Niu & Zhang, 2024).

Flow control devices, which are used to regulate and optimise the flow of fluids in engineering applications, come in a wide range of components, from simple connectors to complex pumps (Yazici et al., 2024), including valves, orifice plates, ventures, and ejectors. Previous studies have investigated the internal flow dynamics and temperature distributions of ejectors with different throat diameters (Kuo et al., 2023). For instance, Samsam et al. (2023) conducted a basic ejector design with computational fluid dynamics (CFD) analysis and achieved a 33% improvement in efficiency through optimisation. They calculated recovery efficiencies at diameters of 0.5, 0.7, and 1 mm under 340 kPa, finding that the 0.5 mm diameter exhibited the highest efficiency at 59%. Similarly, Hemidi et al. (2009) conducted a CFD study using two turbulence models to determine the optimal location of the supersonic ejector throat and identified the k-ε model as yielding the most accurate results.

In other research, Niu and Zhang (2024) optimised the design of vacuum ejectors to improve efficiency, proposing a model that can switch between single and dual ejectors, while Koirala et al. (2021) examined the performance of ejectors in water desalination systems and highlighted their potential for water treatment applications. Besagni et al. (2021) analysed the effects of ejectors on refrigerants, emphasising the development of current uses compared to previous applications. Additionally, Udroiu et al. (2023) proposed adding an ejector to a cascade system to achieve efficiency improvements. Dadpour et al. (2022) studied the effects of secondary liquid droplets in steam ejectors, finding that the addition of droplets had a significant impact on the entrainment ratio and reduced the air suction capacity by 23%. Similarly, Feng et al. (2024) investigated the effects of primary flow droplets on the condensation process, finding that an increase in droplet mass ratio delayed nucleation.

Tavakoli et al. (2023) used a new fluid oscillator to improve ejector performance, increasing the entrainment ratio by 38.3%. Li et al. (2024) compared single-hole and multi-hole ejectors, concluding that multi-hole ejectors provided better mixing efficiency and higher entrainment ratios. Niu and Zhang (2024) conducted a systematic optimisation study on vacuum ejectors, finding that dual ejectors improved efficiency (Niu & Zhang, 2024). Talebiyan et al. (2024) employed adjoint optimisation to improve the geometry of supersonic ejectors, achieving a 20.8% increase in entrainment ratio (Talebiyan et al., 2024).

In theoretical research, Sadeghiseraji et al. (2024) comprehensively reviewed recent advancements in vacuum ejector CFD simulations, highlighting the need for advanced turbulence modelling and the use of machine learning for future ejector designs. Chen et al. (2017) presented a theoretical calculation method to assess the performance of ejector cooling systems, concluding that their models performed better than ejectors operating under the ideal gas law.

Sun et al. (2022) explored highly efficient distillation systems using thermal vapour compression and discovered that a two-stage vacuum ejector can enhance system efficiency by regulating the condensation temperature and removing non-condensable gases. Hwang et al. (2015) analysed ejectors numerically and experimentally for recovering anode outlet gas in fuel cells. Saini et al. (2018) employed an ejector system for air filtration to prevent air pollution and filter out air. Akterina (2011) examined the energy efficiency of vacuum ejectors. Additional extensive research has been conducted by several authors (Thongtip & Aphornratana, 2017; Gullo et al., 2018; Palacz et al., 2018; Ramesh & Sekhar, 2018; Besagni, 2019; Han et al., 2019; Metin et al., 2019; Xue et al., 2020; Ghorbanian & Nejad, 2011).

The present study focuses on the experimental and numerical investigation of a vacuum ejector used in dynamic-function vehicle tyre air control valves. This study aims to enhance the understanding of the ejector performance characteristics and optimise its design for efficient operation in practical applications. Specifically, the influence of key geometric parameters on the ejector's performance, such as nozzle diameter and mixing chamber dimensions, is investigated to identify design configurations that minimise air consumption while maintaining adequate vacuum levels.

2. EXPERIMENTAL STUDIES

This study employed the vacuum ejector depicted in Fig. 1 (Altan Hydraulic Engineering Industry and Trade, Inc.). Initial experimental investigations were conducted to measure the vacuum generated by the vacuum ejector at various flow rates (40, 50, 60, 70, 80, 90, 100, 110, and 120 L/min). Following the experimental analysis, we

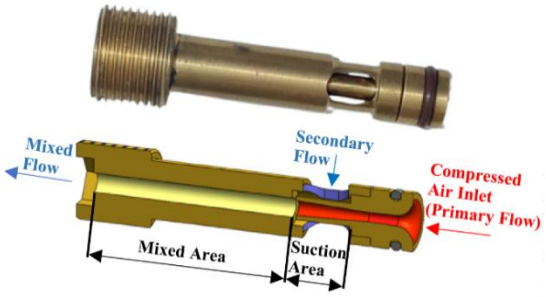

Fig. 1 Vacuum ejector

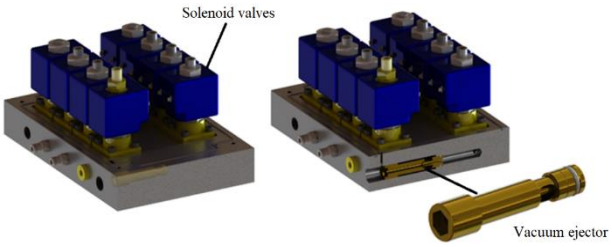

Fig. 2 Position of the vacuum ejector on the pneumatic block

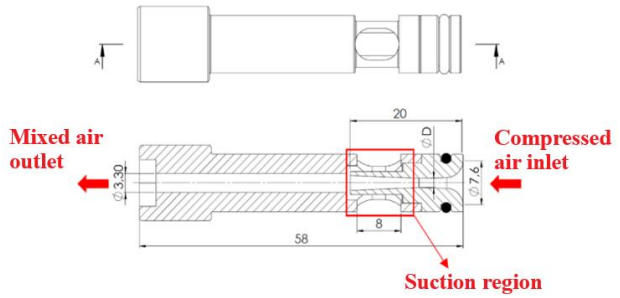

Fig. 3 Dimensions of the vacuum ejector (mm)

carried out numerical simulations to validate the experimental results. In the subsequent phase, a detailed flow analysis was performed on the vacuum ejector by varying the diameter of the constriction section, restricting airflow to evaluate the resulting vacuum.

Figure 2 illustrates the position of the vacuum ejector within the pneumatic control system block. We installed solenoid valves between the vacuum ejector and the tyre valve, with each solenoid valve controlling the airflow to a specific tyre. When air evacuation from the tyre was required, the corresponding solenoid valve was activated, establishing a connection with the vacuum ejector. Additionally, a pressure sensor on the pneumatic control block would prevent air from escaping by closing the solenoid valve once the tyre pressure reached the desired set point.

Figure 3 presents the dimensions of the vacuum ejector. Compressed air entered the vacuum ejector through a Ø7.6 mm inlet. It was then constricted to a diameter *D* to increase its velocity, which facilitated the suction of air from the tyre valve across an 8 mm gap. Finally, the mixed pressurised air was expelled from the ejector. The original vacuum ejector had a constriction diameter *D* of 1.2 mm.

In the experiments, we connected the vacuum ejector to the setup, as shown in Fig. 4. Vacuum pressure was measured at airflow rates of 40, 50, 60, 70, 80, 90, 100, 110, and 120 L/min using an Ashcroft DG25 digital pressure gauge (with a range of 0 to 200 psi, ±0.5% accuracy). Flow measurements were taken using Festo's SFAB600U flow sensor (with a range of 6 to 600 L/min).

The test setup consisted of a block connecting the vacuum ejector, a flow meter, and a vacuum gauge. Compressed air entered the block and passed through the vacuum ejector, undergoing constriction before being

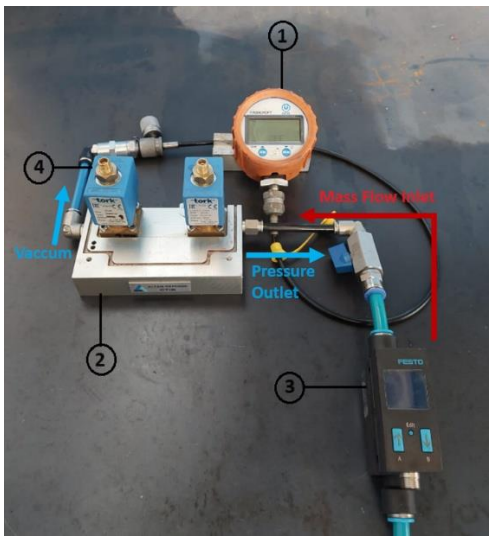

Fig. 4 Vacuum ejector test setup. 1) Vacuum gauge 2) Flow meter 3) Vacuum ejector connection block 4) Solenoid Valve

expelled through the block. The pneumatic control block used in the test setup was equipped with two solenoid valves. Compressed air from the central network was directed to the pneumatic control block, guiding it to the pressure inlet of the vacuum ejector. The pressurised air passing through the vacuum ejector was then expelled through the pneumatic control block. For the reliability and accuracy of the experimental results, the experiments were conducted 3-5 times, and the obtained results were systematically cross-verified for consistency.

3. THEORETICAL MODEL

The theoretical model for the vacuum ejector is developed using equations from Dessouky et al. (2002), Guo et al. (2016), and Niu and Zhang (2024) under several key assumptions (Tang et al., 2017). The flow regions utilised in the mathematical modelling are shown in Fig. 5. The following assumptions are made:

1. The fluid behaves as an ideal gas.
2. The flow is one-dimensional, compressible, and isentropic.
3. The fluid reaches the sonic velocity at the nozzle outlet.
4. The inlet velocities of the primary and secondary fluids were negligible.

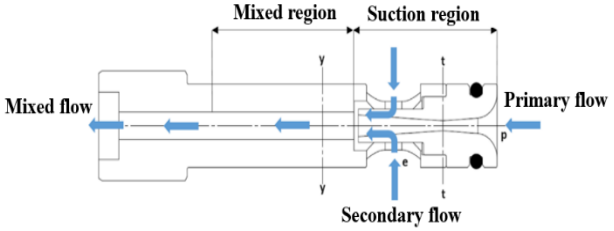

Fig. 5 Flow regions of the vacuum ejector

Assuming that the air pressure through the vacuum ejector is constant and the pressure in the vacuum chamber decreases to achieve sonic velocity at the nozzle throat, the mass flow rate through the nozzle can be described by Eq. (1) (Niu & Zhang, 2024):

$$\dot{m}_p = 1000 P_p A_t \sqrt{\frac{k}{RT_p}\left(\frac{2}{k+1}\right)^{\frac{k+1}{k-1}}\eta_p} \tag{1}$$

where $\dot{m}_p$ is the mass flow rate (kg/s), P_p is the inlet pressure (kPa), k is the isentropic index, A_t is the throat area of the nozzle (mm^2), T_p is the air source temperature (K), R is the gas constant, and η_p is the isentropic efficiency factor.

Equation (1) indicates that the air consumption is directly proportional to the inlet pressure in a vacuum ejector. Furthermore, a 100 kPa reduction in the inlet pressure (which generates the vacuum) results in a 4–6% decrease in the compressor's power consumption. Consequently, operating with lower inlet pressures can lead to energy savings. By analysing the fluid flow from the nozzle inlet to the outlet, the following equations are derived (Niu & Zhang, 2024):

$$\frac{A_{p1}}{A_t} = \frac{1}{M_{p1}}\left[\frac{2}{k+1}\left(1+\frac{k-1}{2}M_{p1}^2\right)\right]^{\frac{k+1}{2(k-1)}} \tag{2}$$

$$\frac{P_p}{P_{p1}} = \left(1+\frac{k-1}{2}M_{p1}^2\right)^{\frac{k}{(k-1)}} \tag{3}$$

where A_{p1} is the nozzle exit area (mm^2), M_{p1} is the Mach number at the nozzle exit, and P_{p1} is the pressure at the nozzle exit (kPa).

The equation for the fluid at the y-y section formed after the nozzle exit is expressed in Eq. (4):

$$\frac{A_{py}}{A_{p1}} = \frac{M_{p1}\left[\frac{2}{k+1}\left(1+\frac{k-1}{2}M_{py}^2\right)\right]^{\frac{k+1}{2(k-1)}}}{Mpy\left[\frac{2}{k+1}\left(1+\frac{k-1}{2}M_{p1}^2\right)\right]^{\frac{k+1}{2(k-1)}}}\eta_{py} \tag{4}$$

$$\frac{P_{py}}{P_{p1}} = \frac{\left(1+\frac{k-1}{2}M_{p1}^2\right)^{\frac{k}{(k-1)}}}{\left(1+\frac{k-1}{2}M_{py}^2\right)^{\frac{k}{(k-1)}}} \tag{5}$$

where A_{py} is the area of the y-y section (mm^2), M_{py} is the Mach number in the y section, P_{py} is the fluid pressure in the y-y section (kPa), and η_{py} is the isentropic efficiency factor.

The equation for the fluid in the y-y section formed after the vacuum region is expressed as

$$\frac{P_{se}}{P_{sy}} = \left(1+\frac{k-1}{2}M_{sy}^2\right)^{\frac{k}{(k-1)}} \tag{6}$$

where P_{se} is the fluid pressure at the e-section, P_{sy} is the fluid pressure at the y-y section, and M_{sy} is the Mach number at the y-y section.

The mass flow rate equation at the vacuum port is expressed as follows:

$$\dot{m}_s = 1000 P_{se} A_{sy} \sqrt{\eta_s \frac{k}{RT_{se}}\left(\frac{2}{k+1}\right)^{\frac{k+1}{k-1}}} \tag{7}$$

where A_{sy} is the area of the induced flow at cross-section y-y (mm^2), T_{se} is the inlet temperature of induced flow (K).

The theoretical analysis shows that the pressure ratio in each section is related to the Mach number and influenced by the area ratio. Consequently, modifying the area ratios in each section changes the internal flow area of the vacuum ejector (Niu & Zhang, 2024).

4. NUMERICAL STUDIES

In the numerical studies, we initially investigated a vacuum ejector with a throat diameter of 1.2 mm, the same as that used in the experimental studies. Reynolds numbers (Re), determined based on the flow rates used in the experiments (i.e., 40, 50, 60, 70, 80, 90, 100, 110, and 120 L/min), were calculated as 11,442; 14,302; 17,163; 20,023; 22,884; 25,744; 28,605; 31,465; and 34,326, respectively. We varied the throat diameter of the vacuum ejector from 0.2 to 1.6 mm in increments of 0.2 mm and calculated the corresponding vacuum values. The selection of these throat diameters was based on the ejector used in the experimental study with a throat diameter of 1.2 mm, and the literature advises against using throat diameters of <1 mm (Hwang et al., 2015).

The numerical simulations were conducted using Simcenter Star CCM+ software, a robust and versatile tool for fluid dynamics analysis. We employed the finite volume method for spatial discretisation of the governing equations, providing a reliable framework for capturing the complex flow behaviour within the vacuum ejector. A second-order upwind scheme was applied to achieve accuracy in resolving flow gradients, particularly in regions with sharp changes, such as the nozzle throat and mixing chamber. To capture compressible flow phenomena—such as shock waves and rapid density gradients—a density-based coupled solver was employed (Siemens, 2023). This solver simultaneously addresses the governing equations of mass, momentum, and energy, making it particularly effective for stiff compressible flow regimes. Additionally, the ideal gas law was applied to model density variations, while the inclusion of the energy equation accounted for compressibility effects. Furthermore, we utilised an implicit time-stepping scheme to achieve steady-state solutions efficiently, ensuring computational consistency and robustness throughout the analysis.

The mass (Eq. (8)) and momentum (Eq. (9)) for compressible fluid flows (Navier–Stokes equations) were numerically solved to model the flow phenomenon. The k-ε turbulence model was used for the numerical solutions (Eqs. (10) and (11)). Hemidi et al. (2009) found that the k-ε model provided results superior to those of other turbulence models in the literature. However, the selection of the most suitable model remains an ongoing area of research.

Despite the predominance of Reynolds-averaged Navier–Stokes (RANS)-based turbulence models in recent years, the use of large eddy simulation (LES) by Zaheer and Masud (2017) and Croquer et al. (2022) is noteworthy. Among the RANS-based turbulence models, the *k-ω* shear stress transport (SST) model (Wen et al., 2020; Niu & Zhang, 2024; Li et al., 2024; Talebiyan et al., 2024; Tavakoli et al., 2023) has been favoured for capturing flow characteristics inside ejectors, showing stronger performance than other turbulence models. However, some studies have used the standard *k-ε* model (Tavakoli et al., 2023; Chai et al., 2024) and the realisable k-ε model (Hou et al., 2022; Ariafar et al., 2015) in their simulations. Notably, Tavakoli et al. (2023) reported no significant differences between the results obtained using the *k-ω* SST model and the standard *k-ε* model. The *k-ε* model has also provided good result in incompressible flows (Kibar et al., 2025).

Accordingly, the mass conservation equation is as follows:

$$\frac{\partial \rho}{\partial t} + \nabla \cdot \left(\rho \vec{V}\right) = 0 \tag{8}$$

The momentum conservation equation is as follows:

$$\frac{\partial (\rho \overrightarrow{V})}{\partial t} + \nabla \cdot \left(\rho \vec{V} \vec{V}\right) = -\nabla p + \nabla \cdot \tau \tag{9}$$

Equation (10) represents the conservation equation for the turbulent kinetic energy *k*, while Eq. (11) represents the conservation equation for the rate of turbulent kinetic energy dissipation *ε*.

$$\frac{\partial(\rho k)}{\partial t} + \frac{\partial}{\partial x_i}.(\rho k u_i) = \frac{\partial}{\partial x_j}\left[\left(\mu + \frac{\mu_t}{\sigma_k}\right)\frac{\partial k}{\partial x_j}\right] + G_k + G_b - \rho\varepsilon - \Phi_k \tag{10}$$

$$\frac{\partial(\rho \varepsilon)}{\partial t} + \frac{\partial}{\partial x_i}.(\rho \varepsilon u_i) = \frac{\partial}{\partial x_j}\left[\left(\mu + \frac{\mu_t}{\sigma_\varepsilon}\right)\frac{\partial \varepsilon}{\partial x_j}\right] + C_1 \frac{\varepsilon}{k}(G_k + C_3 G_b) - C_2 \rho \frac{\varepsilon^2}{k + \sqrt{\vartheta \varepsilon}} - \Phi_\varepsilon \tag{11}$$

where μ_t is the turbulent viscosity, σ_k and σ_ε are model constants, C_1 and C_2 are empirical constants in the model, C_3 additional coefficient varying at high Mach numbers, G_k signifies the generation of turbulent kinetic energy resulting from mean velocity gradients. G_b additional production term arising from thermal and density variations, Φ_k additional energy dissipation term due to compressibility and Φ_ε additional destruction term due to compressibility

Equation (12) represents the conservation equation for the turbulent kinetic energy *k*, which describes the production, diffusion, and dissipation of turbulence in the flow. The dissipation of turbulent kinetic energy is modelled as proportional to the specific dissipation rate *ω*. Equation (13) represents the conservation equation for the specific dissipation rate *ω*, which governs how quickly the turbulent kinetic energy dissipates. This equation includes terms for production, diffusion, and dissipation of *ω*, as well as a cross-diffusion term that ensures a smooth transition between the *k-ε* and *k-ω* models in different regions of the flow. Together, these equations form the *k-ω* SST model, which is particularly effective in capturing both boundary layer and free-shear flow phenomena.

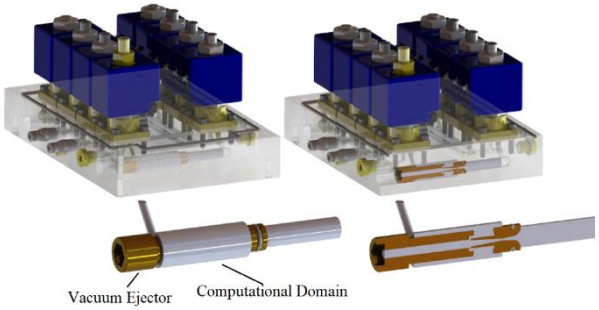

(a) (b)

Fig. 6 a) Vacuum ejector and computational domain. b) Cross-sectional view of vacuum ejector and computational domain

$$\frac{\partial(\rho k)}{\partial t} + \frac{\partial}{\partial x_i}.(\rho k u_i) = \frac{\partial}{\partial x_j}\left[\left(\mu + \frac{\mu_t}{\sigma_k}\right)\frac{\partial k}{\partial x_j}\right] + P_k - \beta^* \rho \omega k \tag{12}$$

$$\frac{\partial(\rho \varepsilon)}{\partial t} + \frac{\partial}{\partial x_i}.(\rho \omega u_i) = \frac{\partial}{\partial x_j}\left[\left(\mu + \frac{\mu_t}{\sigma_\omega}\right)\frac{\partial \omega}{\partial x_j}\right] + \alpha \frac{\omega}{k} P_k - \beta \rho \omega^2 + 2(1 - F_1)\rho \sigma_{\omega 2} \frac{1}{\omega}\frac{\partial k}{\partial x_j}\frac{\partial \omega}{\partial x_j} \tag{13}$$

where μ_t turbulent viscosity, σ_k model constant for turbulent kinetic energy, β^* model constant (typically 0.09), $\rho\omega k$ dissipation of turbulent kinetic energy, proportional to the specific dissipation rate (ω), σ_ω is the model constant for specific dissipation rate, α is model constants (typically 5/9), β is model constant (typically 0.075), F_1 blending function that transitions between *k-ε* and *k-ω* models, $\sigma_{\omega 2}$ model constant for the cross-diffusion term.

4.1 Geometric Model and Boundary Conditions

We created 3D models of the vacuum ejector using SolidWorks. Figure 6 illustrates the vacuum ejector and the computational domain, which is defined as the area between the pneumatic block and the vacuum ejector. This region encompasses areas where pressurised air enters the vacuum ejector from the block, mixes with the air from the tyre valve, and exits as a combined air output under vacuum.

The locations of the constriction (nozzle), nozzle exit area, and throat diameter are critical parameters that influence the design of the ejector (Kuo et al., 2023). Figure 7 shows the vacuum ejectors used in the numerical analysis. The original vacuum ejector had a constriction diameter of 1.2 mm. Initially, we conducted numerical studies on the original vacuum ejector, then varied the constriction diameter to analyse the impact on the vacuum value. In total, we performed 72 numerical analysis studies, which involved a vacuum ejector with nine Re values and eight constriction diameters.

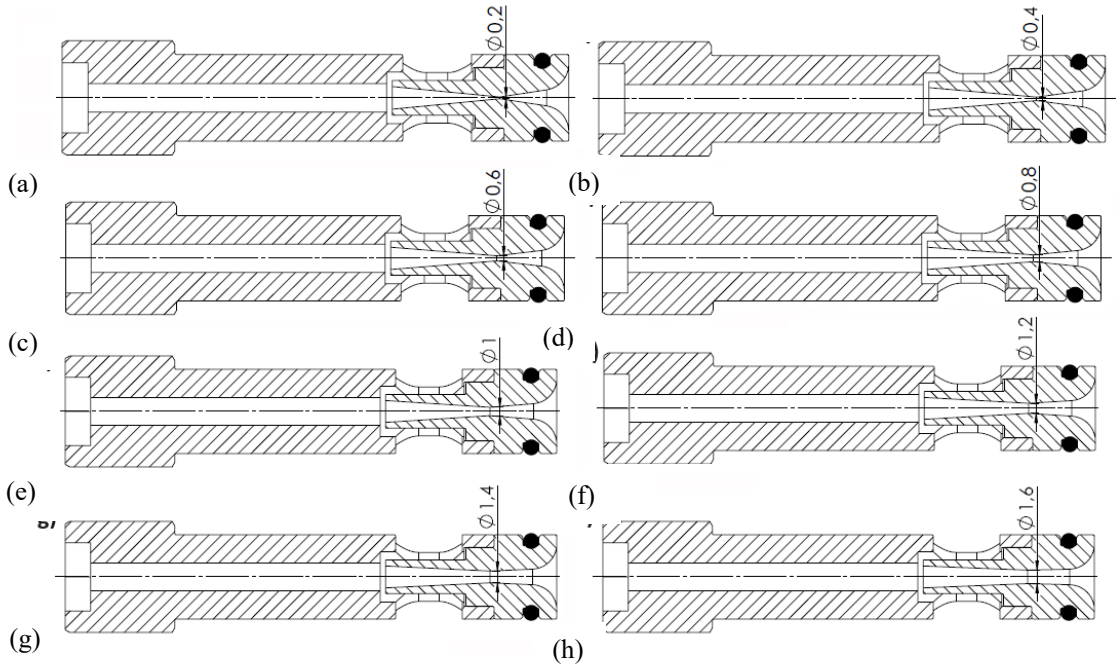

Fig. 7 Vacuum ejectors with constriction diameters of a) 0.2, b) 0.4, c) 0.6, d) 0.8, e) 1, f) 1.2, g) 1.4, and h) 1.6 mm

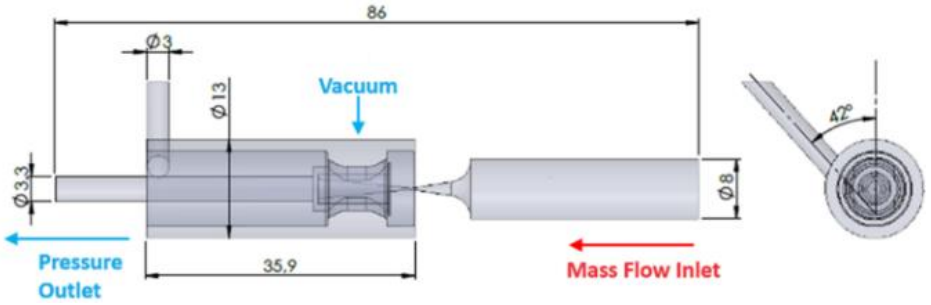

Fig. 8 Computational domain dimensions (mm)

Figure 8 shows the dimensions of the computational domain. Air enters through an Ø8 mm inlet, narrows down, and then moves from the tyre valve area, reaching the vacuum region. The mixed air then exits through an outlet with a diameter of 3.3 mm.

4.2 Mesh Domain and Mesh Independence

For the numerical studies on the vacuum ejector, we opted for a polyhedral mesh. Five mesh densities were analysed to determine the optimal number of cells (Table 1). Figure 9 illustrates the polyhedral mesh structure used in the numerical studies on the vacuum ejector. Table 1 presents the base size values used in the numerical studies. The base size was reduced by approximately 10% in critical areas.

Figure 10 shows the vacuum values obtained for the five mesh sizes along with the experimental results. The results show similar values in general, although some discrepancies between the cases and the experimental results are evident. These differences fall within an acceptable margin of error. Based on these findings, Case V, which contained the most cells and showed the closest

Table 1 Number of cells in different cases

Case	Number of Cells	Base Size (mm)
I	101,500	0.75
II	131,716	0.60
III	178,078	0.50
IV	248,691	0.40
V	329,959	0.32

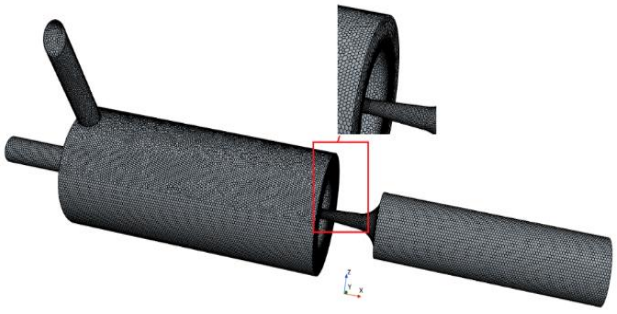

Fig. 9 Polyhedral mesh structure used in numerical studies of the vacuum ejector

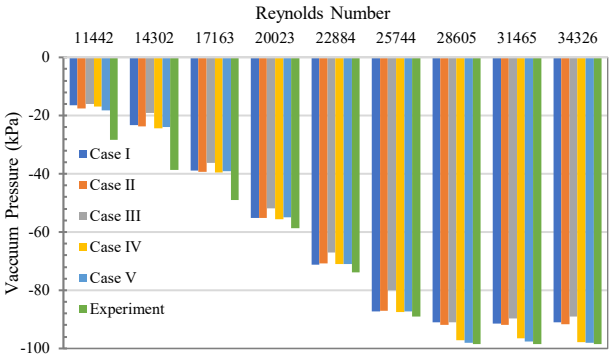

Fig. 10 Comparison of vacuum values for different mesh sizes with experimental study results

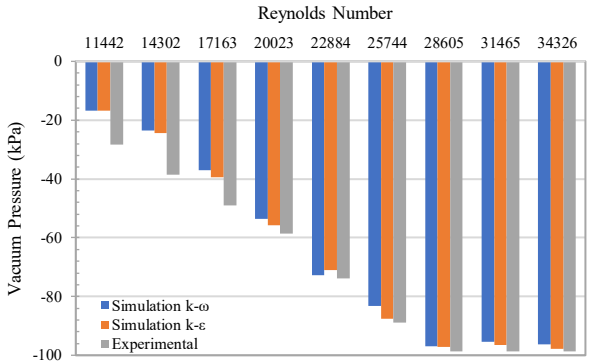

Fig. 11 Experimental and numerical vacuum pressures

alignment with the experimental results, was selected for the simulation studies.

5. RESULT AND DISCUSSION

Figure 11 compares the experimental and numerical results (k-ε and k-ω SST) of the vacuum ejector with a contraction diameter of 1.2 mm. The results indicate that the outcomes obtained from the k-ε and k-ω SST turbulence models are close to each other. In this study, the k-ε model was selected for its practicality and computational efficiency in providing fast results. The disparity between experimental and numerical results is significant at lower Re but narrows as the Re increases. Moreover, both the experimental and numerical results closely approach the maximum vacuum pressure of −100 kPa when Re reaches ~28,600, which is considered critical, as exceeding it can result in unnecessary energy loss.

Figure 12 illustrates the vacuum pressures observed at Re values of 11,442; 20,023; 28,605; and 34,326 for throat diameters of 0.4, 0.6, 0.8, 1, 1.2, 1.4, and 1.6 mm. For Reynolds numbers 11,442 and 20,023, the largest vacuum pressures occur with a throat diameter of 1 mm. At Re = 28,605 and 34,326, 1 and 1.2 mm throat diameters yield similar results, while 1.4 and 1.6 mm produce the lowest vacuum pressures across all Reynolds numbers.

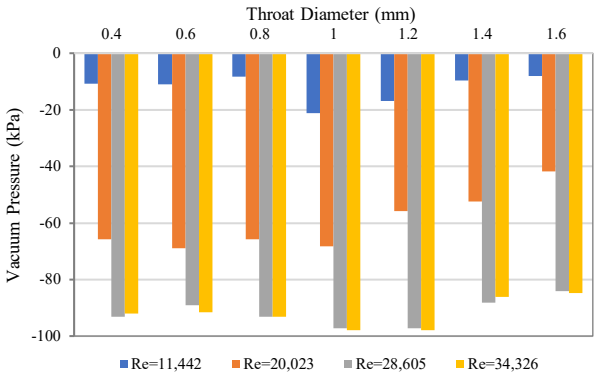

Fig. 12 Vacuum pressures at different throat diameters

For throat diameters <1 mm, at Re = 11,442 and 20,023, the vacuum pressure initially increases and then decreases. Normally, as the throat diameter narrows, velocity increases, which should lead to an increase in vacuum pressure; however, the opposite occurs here, indicating flow instability.

A throat diameter of 0.2 mm was also considered in the analysis studies, but flow could not be sustained at this diameter, resulting in choking; hence, it is not included in Fig. 12. The throat diameters of 1 and 1.2 mm are the closest to achieving a vacuum pressure of −100 kPa. However, at Re = 20,023, the 1.2 mm throat diameter yields a vacuum of −55.7 kPa, while a vacuum of −68.3 kPa occurs with a throat diameter of 1 mm. Similarly, at Re = 11,442, a vacuum of −16.8 kPa is achieved with a nozzle throat of 1.2 mm, while a vacuum of −21.1 kPa results from a throat diameter of 1 mm. For other throat diameters, the vacuum pressures are lower than those at 1 mm. At Re = 28,605, the vacuum pressure approaches −100 kPa with a value of −97.2 kPa for throat diameters of 1 and 1.2 mm. The highest vacuum pressure of −98.6 kPa was achieved in the experimental study at Ø1 mm, which aligns well with the highest vacuum pressures in the simulations (−97.9 kPa) at Re = 34,326.

Figure 13 plots the variation in experimental and theoretical mass flow rates with Re. The theoretical

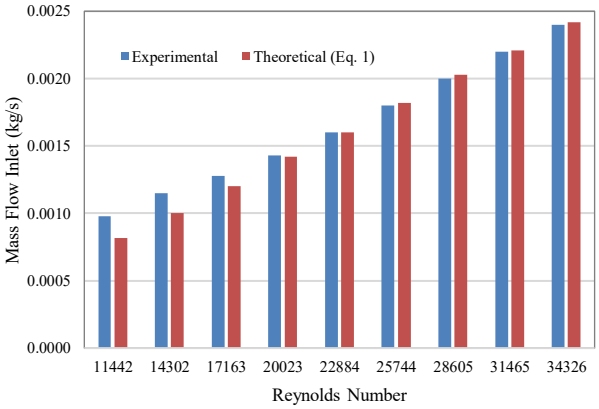

Fig. 13 Variation between experimental and theoretical mass flow rates according to Renumber for a nozzle throat diameter of 1.2 mm

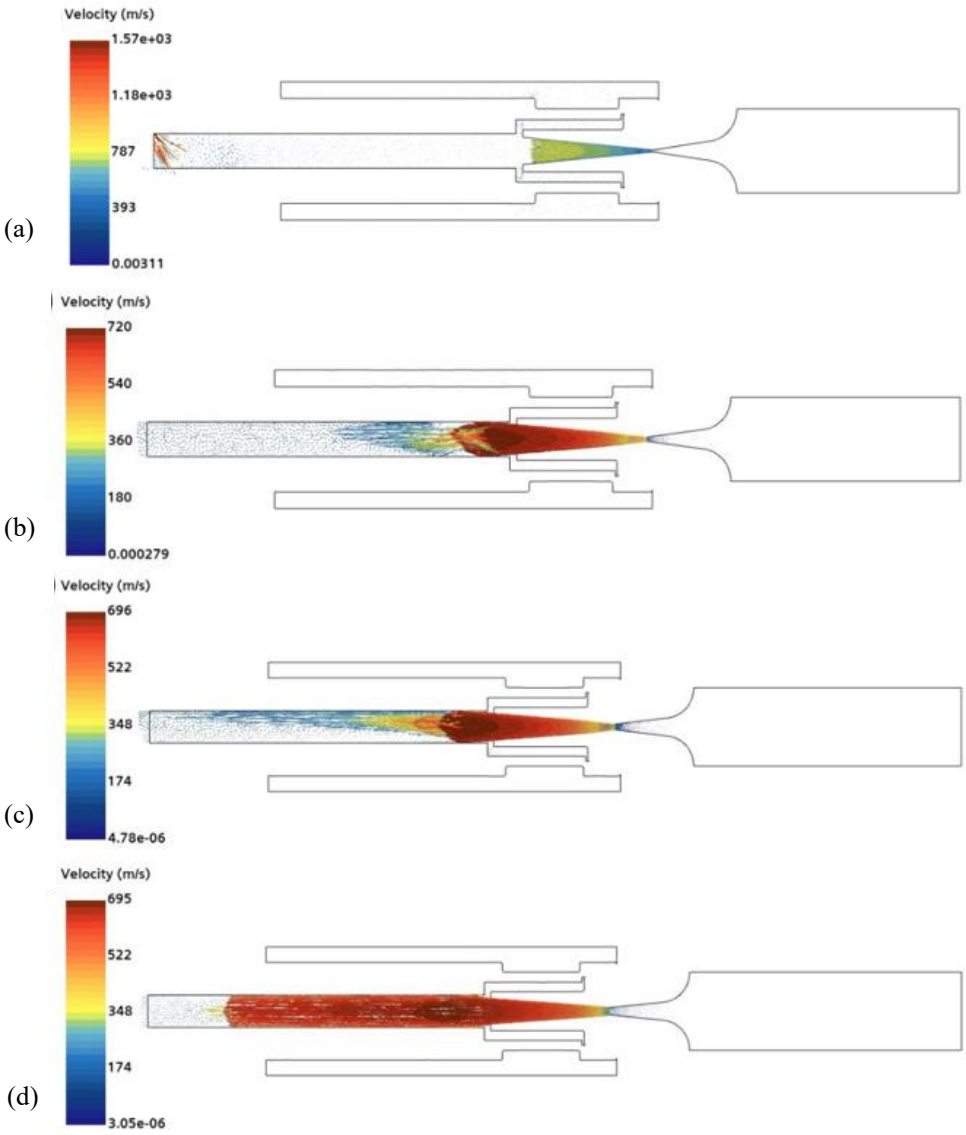

Fig. 14 Velocity vectors for a) 0.2, b) 0.4, c) 0.6, and d) 0.8 mm nozzle diameters

calculations are based on Eq. (1). While a significant difference is evident between the experimental and theoretical flow rates at low Re, this difference gradually decreases as Re increases. At Re > ~20,000, the two flow rates are very similar. Therefore, the mathematical model has been validated through both experimental and numerical results.

Figure 14 shows the velocity vectors for contraction diameters ranging from 0.2 to 0.8 mm. According to Bernoulli's principle, the flow velocity increases as the fluid channel narrows and decreases as the channel widens. For smaller diameters (ranging from 0.2 to 0.8 mm), the velocity remains relatively constant until the fluid exits the ejector. However, as the contraction diameter increases, a more noticeable decrease in velocity occurs downstream. The highest velocities are near the contraction region, where the fluid accelerates despite the reduced flow quantity. Critically, the flow is fully choked at a 0.2 mm diameter (Fig. 14a). In Fig. 14b, with a throat diameter of 0.4 mm, the flow begins to accelerate after the throat, reaching 720 m/s at the nozzle exit. However, after this acceleration, the velocity begins to decrease sharply. The same phenomenon happens with a 0.6 mm throat diameter (Fig. 14c). In Fig. 14d, with a throat diameter of 0.8 mm, the fluid velocity reaches its maximum at the nozzle exit, maintains this high value for a significant distance near the ejector exit, and then experiences a sudden drop.

Figure 15 shows the velocities of the ejector sections with throat diameters of 1, 1.2, 1.4, and 1.6 mm. In Fig. 15a, the velocity distribution for a 1 mm throat diameter reveals that the fluid reaches its highest velocity at the nozzle exit and maintains this speed up to a region close to the ejector exit, where the velocity then decreases. In Figs. 15b, c, and d for 1.2, 1.4, and 1.6 mm, respectively, the maximum velocities decrease as the throat diameter increases, with abrupt decreases occurring closer to the nozzle exit. Fig. 15d shows the flow reaching its lowest velocity and experiencing an abrupt drop near the nozzle.

Figure 14d (Ø0.8 mm) shows that the flow velocity is maintained closest to the nozzle exit, while Fig. 15a (Ø1 mm) demonstrates even better velocity retention near

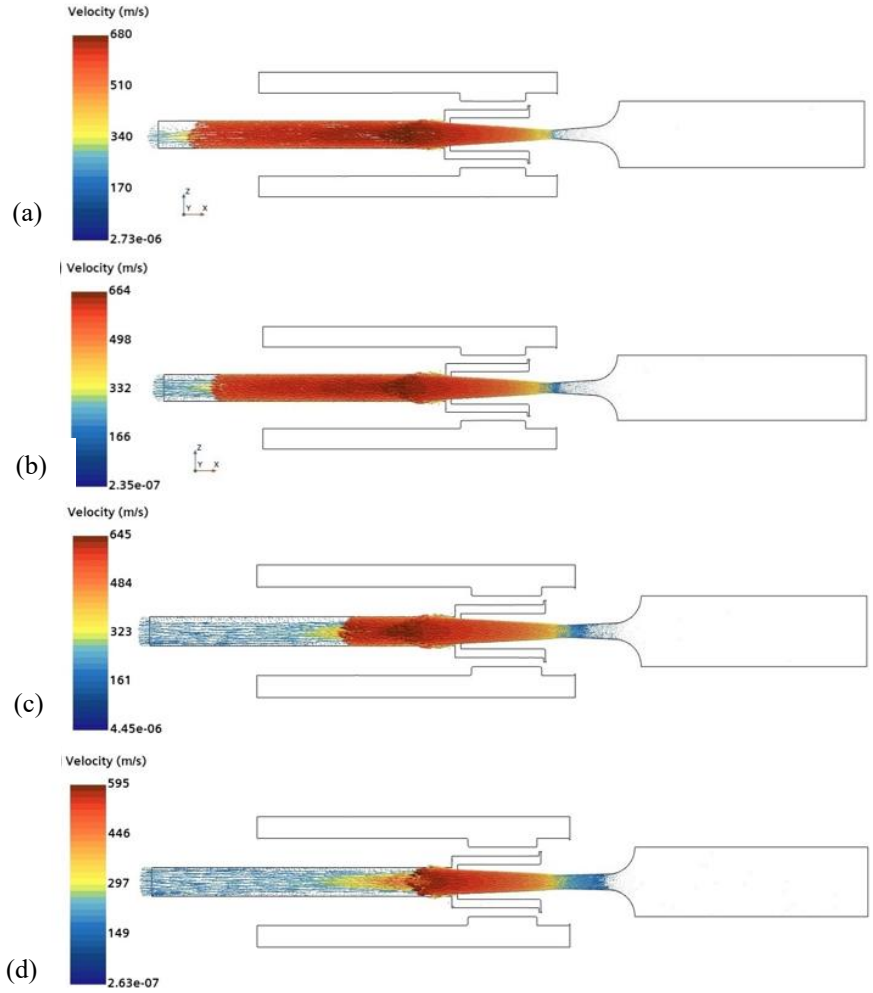

Fig. 15 Velocity vectors for a) 1, b) 1.2, c) 1.4, and d) 1.6 mm nozzle diameters

the ejector exit. Ideally, the fluid velocity should increase at the nozzle inlet, reach its highest speed at the nozzle exit, and maintain this speed until the ejector exits the tank. This behaviour is crucial to generate the highest vacuum pressure in the suction region (Fig. 5) and to sustain this vacuum pressure as much as possible in the mixing region. It ensures that the vacuum ejector continuously performs high levels of air suction and quickly expels the fluid to the external environment. Upon reviewing Figs. 14 and 15, the optimal performance is observed to be at a throat diameter of 1 mm, as shown in Fig. 15a.

Figures 14 and 15 show that as the throat diameter increases, the maximum velocities decrease. Additionally, the pressure values at the inlet of the vacuum ejector, obtained from the numerical simulations, are presented in Table 2 for Re = 28,605. In Fig. 14b (Ø0.4 mm), the maximum flow velocity is 720 m/s, while in Fig. 15d (Ø 1.6 mm), it is 17.4% lower, reaching 595 m/s. The pressure is also lower by 94%, reaching 333 kPa. Accordingly, the increase in the throat diameter results in a significant reduction in the inlet pressure, while the reduction in the flow velocity is much less than that of the pressure.

Table 2 Inlet pressure for Re = 28,605

Throat Diameter (mm)	Inlet Pressure (kPa)
0.4	5570
0.6	2400
0.8	1490
1.0	988
1.2	660
1.4	460
1.6	333

In the experimental studies, the inlet pressure of the ejector was 660 kPa. This value is lower than the pressure produced by air compressors (typically 800−1000 kPa). For a throat diameter of 1 mm, the calculated inlet pressure is closer to this value at 988 kPa. However, inlet pressures achieved with throat diameters of <1 mm exceed this air compressor threshold. As a result, these ejectors may not be suitable in a standard air compressor.

Figure 16 shows the Mach numbers for the range of throat diameters. At entry to the contraction throat, the Mach number is 1 in all cases, indicating that the critical pressure ratio has been exceeded (Cantwell, 2018). As the fluid expands at the nozzle exit, the Mach number

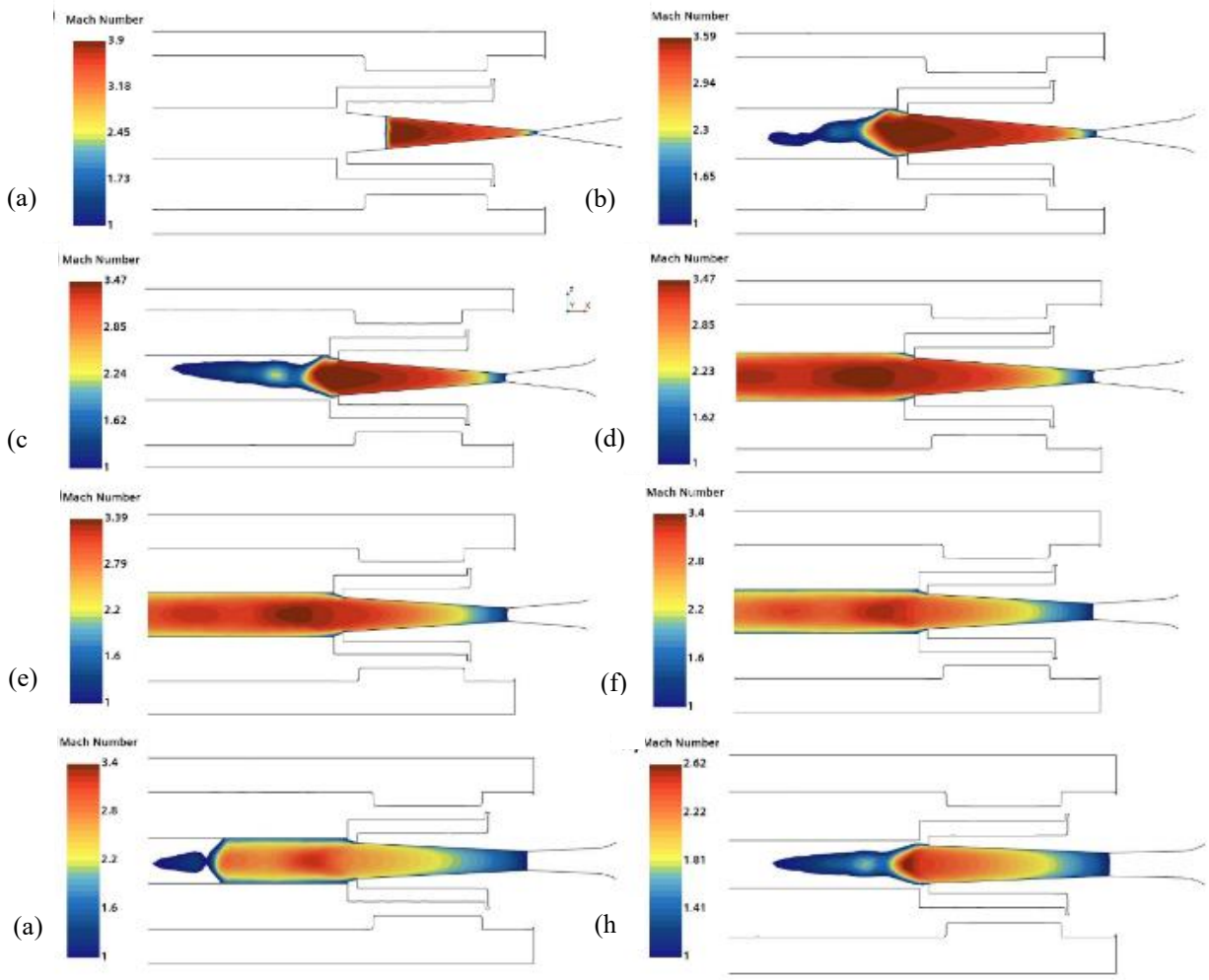

Fig 16. Mach Numbers at constriction throat and nozzle exit for throat diameters of a) 0.2, b) 0.4, c) 0.6, d) 0.8, e) 1, f) 1.2, g) 1.4, and h) 1.6 mm

increases in all cases. In addition, as the throat diameter increases, the Mach number obtained decreases.

However, at throat diameters of 0.4, 0.6, and 1.6 mm, the Mach number does not increase after exiting the nozzle but drops to 1. When the throat diameter is 1.6 mm, Fig. 16h shows that the fluid does not accelerate sufficiently to create adequate vacuum effects. At this diameter, the fluid flows more easily, and the Mach number decreases at the nozzle exit. In Figs. 16b and c, the smaller throat diameters allow the fluid to accelerate but prevent further acceleration upon nozzle exit, resulting in a decrease in the Mach number.

At a throat diameter of 0.2, Fig. 16a shows that the Mach number and, thus, mass flow reach their maximum values. As a result, the fluid cannot pass through the throat, leading to flow choking (Cantwell, 2018). Figs. 16a–c show irregularities because of excessive narrowing in the contraction region, which leads to insufficient vacuum effects and choking.

Figures 16d and e (Ø0.8 and Ø1 mm, respectively) demonstrate the best distribution of Mach numbers, where the fluid continues to accelerate after exiting the nozzle. This outcome is ideal for generating sufficient vacuum pressure. Figure 16 reveals that the best vacuum value occurs at a throat diameter of 1 mm, which aligns with Hwang et al. (2015).

The choking of flow and the increase in Mach number after the throat can be explained by the critical pressure ratio, which is calculated by Eq. (12):

$$\frac{P_t}{P_{ambient}} = \left(\frac{\gamma + 1}{2}\right)^{\frac{\gamma}{\gamma - 1}} \tag{12}$$

where P_t is the pressure at the nozzle inlet, $P_{ambient}$ is the ambient pressure, and γ is Poisson's ratio (γ = 1.4 for air)

The critical pressure ratio for air is 1.893. When the critical pressure ratio reaches this critical value, the Mach number peaks. In this case, the mass flow and temperature of the air passing through the nozzle also peak, and the flow is considered choked (Fig. 14a and Fig. 16a). If the critical pressure ratio exceeds 1.893, the Mach number remains 1, and the flow no longer accelerates.

Figure 17b shows that the Mach number increases up to the narrowest point of the throat and reaches 1 at the throat. In Fig. 17a, the Mach number exceeds 1 at the throat exit and rapidly decreases in the outlet region. The flow begins to expand and attempts to adjust to the ambient pressure. As the flow exits the nozzle, it adjusts

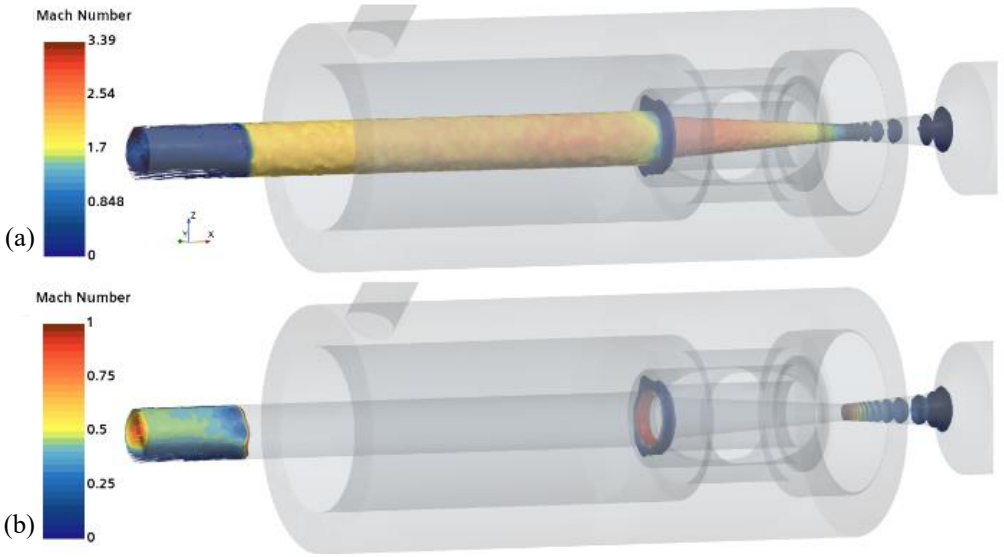

Fig 17. Distribution of the Mach number on the ejector iso-surfaces a) Mach number from 0 to max. value a) Mach number from 0 to 1 value

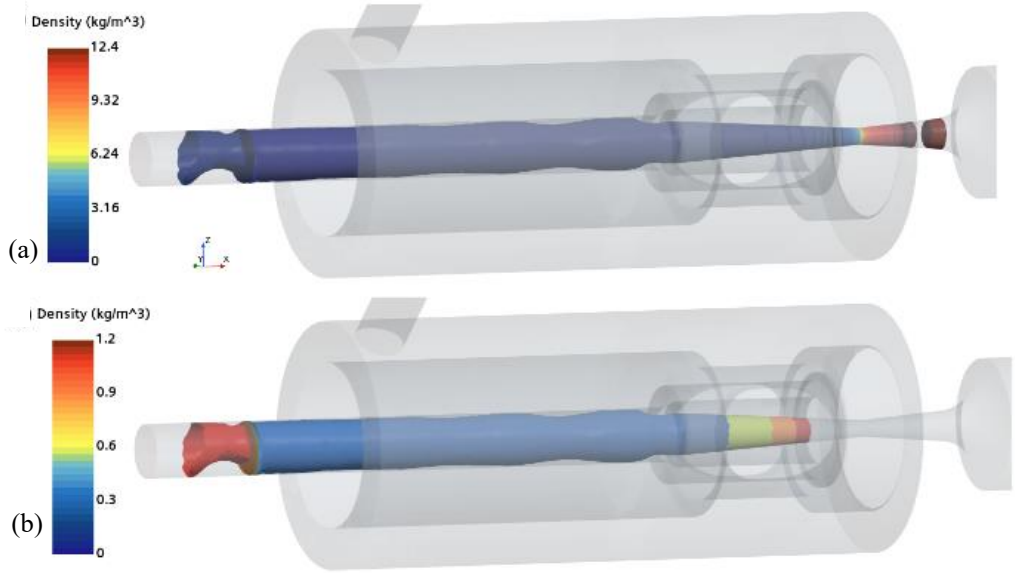

Fig 18. Density at constriction throat and nozzle exit a) Density from 0 to max. value a) Density from 0 to 1.2 value

to the ambient pressure through expansions and shocks (Cantwell, 2018).

Figure 18 illustrates the density variation within the ejector at a throat diameter of 1.0 mm and a Reynolds number of 28,605. In Fig. 18a, the density is in the range of 0 to 12.4 kg/m^3. The fluid reaches its maximum density at the throat entrance. Subsequently, as the flow is constricted within the throat, the density continues to decrease. Once the flow begins to expand in the nozzle section, the density decreases rapidly, approaching zero.

In Fig. 18b, the density of air ranges from 0 to 1.2 kg/m^3. After the constriction, the density reaches 1.2 kg/m^3, then begins to decrease, and at the ejector outlet, it returns to 1.2 kg/m^3. The primary reason for the gradual decrease in density up to the throat region, followed by a rapid decrease after the nozzle, is the Mach number reaching 1 in the throat region and then increasing rapidly. In this case, the significant rise in mass flow rate and temperature causes the air density to decrease rapidly.

Figures 19 and 20 show the temperature and Mach number distributions along the $+x$ direction of the vacuum ejector. In regions where the Mach number increases, the temperature decreases. Where the Mach number is highest, the temperature drops to approximately 100 K. As the Mach number continues to rise, the temperature increases again, reaching around 300 K. This indicates that because of the high velocity of the fluid, thermal energy is converted into kinetic energy (Hwang et al., 2015). At Re = 11,442 in Fig. 19a, the fluid maintains its temperature at 300 K until it reaches the contraction throat.

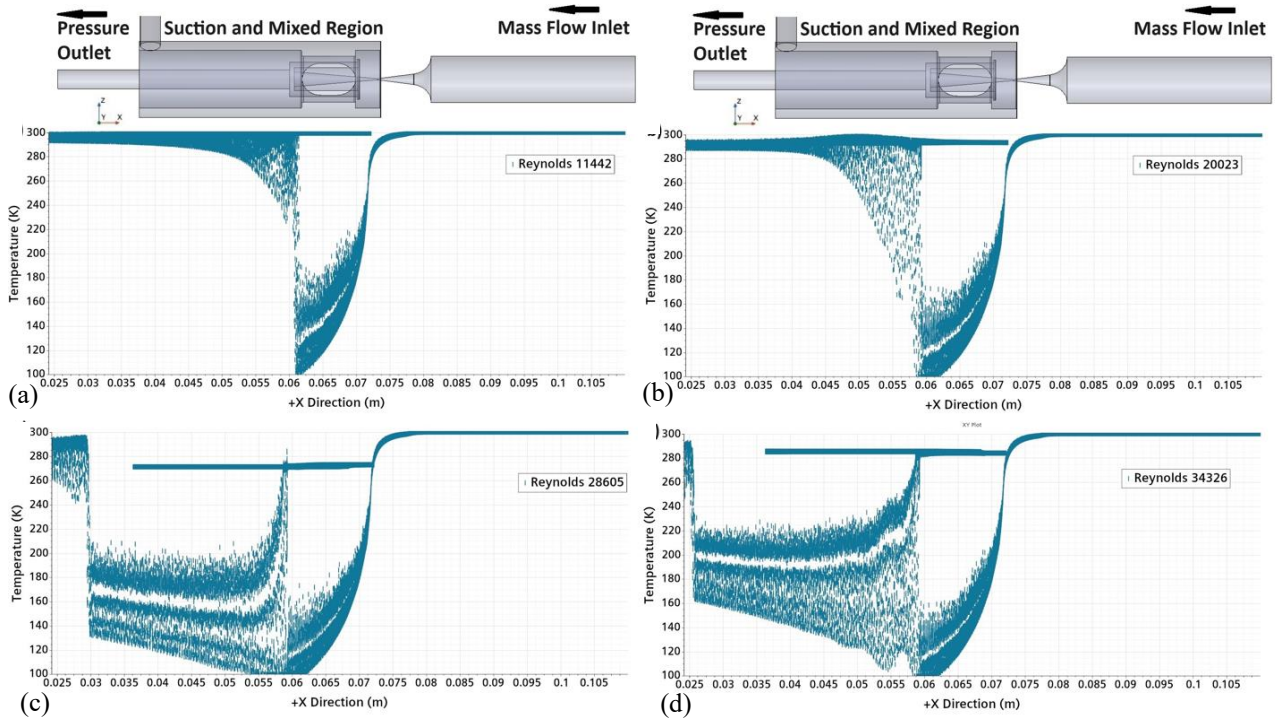

Fig. 19 Temperatures in Ø1 mm constriction vacuum ejector. a) Re = 11,442; b) Re = 20,023; c) Re = 28,605; d) Re = 34,326

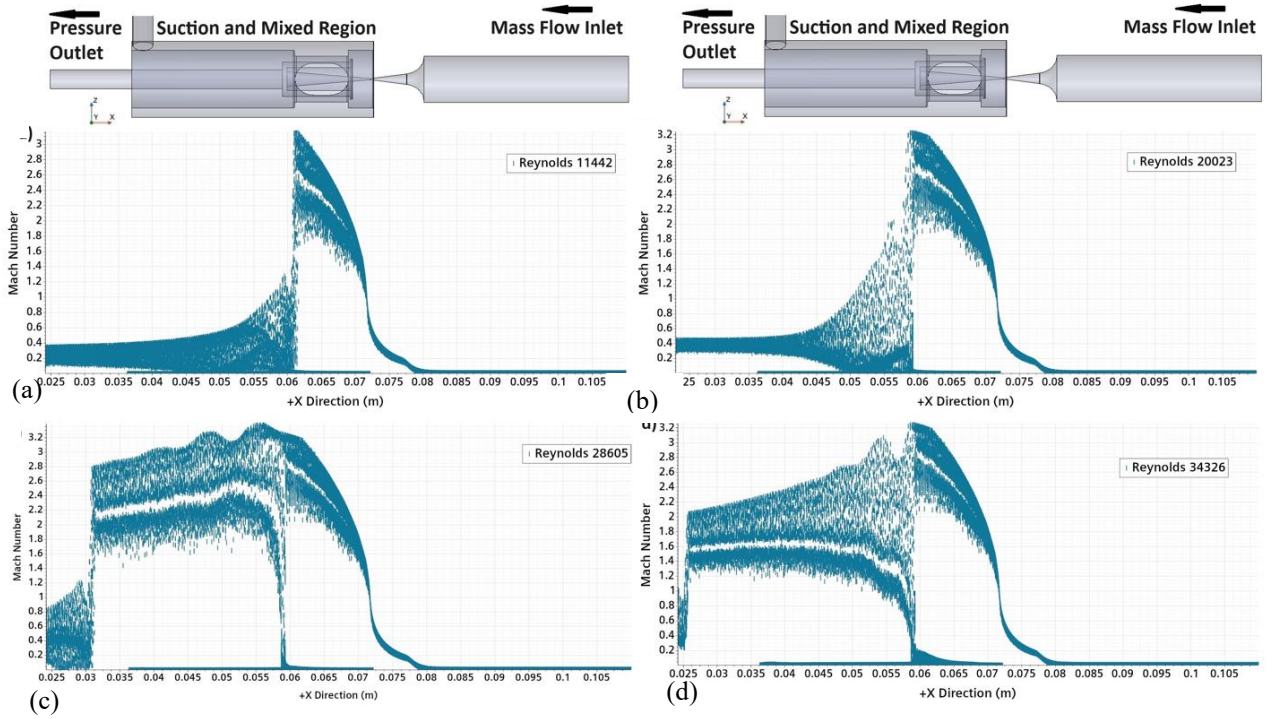

Fig. 20 Mach numbers in Ø1 mm constriction vacuum ejector. a) Re = 11,442, b) Re = 20,023, c) Re = 28,605, and d) Re = 34,326

This result is consistent with other Reynolds numbers, as shown in Fig. 19. Upon reaching the contraction throat, a sudden drop in temperature is evident. For Re = 11,442 (Fig. 19a), the fluid returns to 300 K at the nozzle exit and leaves the ejector at this temperature. In addition, the Mach number of the fluid decreases rapidly to subsonic speeds at the nozzle exit.

As the Reynolds number increases (Fig. 19), the tendency for temperatures to rise again at the nozzle exit diminishes. Consequently, as shown in Fig. 20d, for Re = 34,326, the Mach number maintains a value of 2 up to the ejector exit. Therefore, Figs. 19 and 20 reveal low temperatures and high Mach numbers in the suction and mixing regions. This finding is consistent with the situation

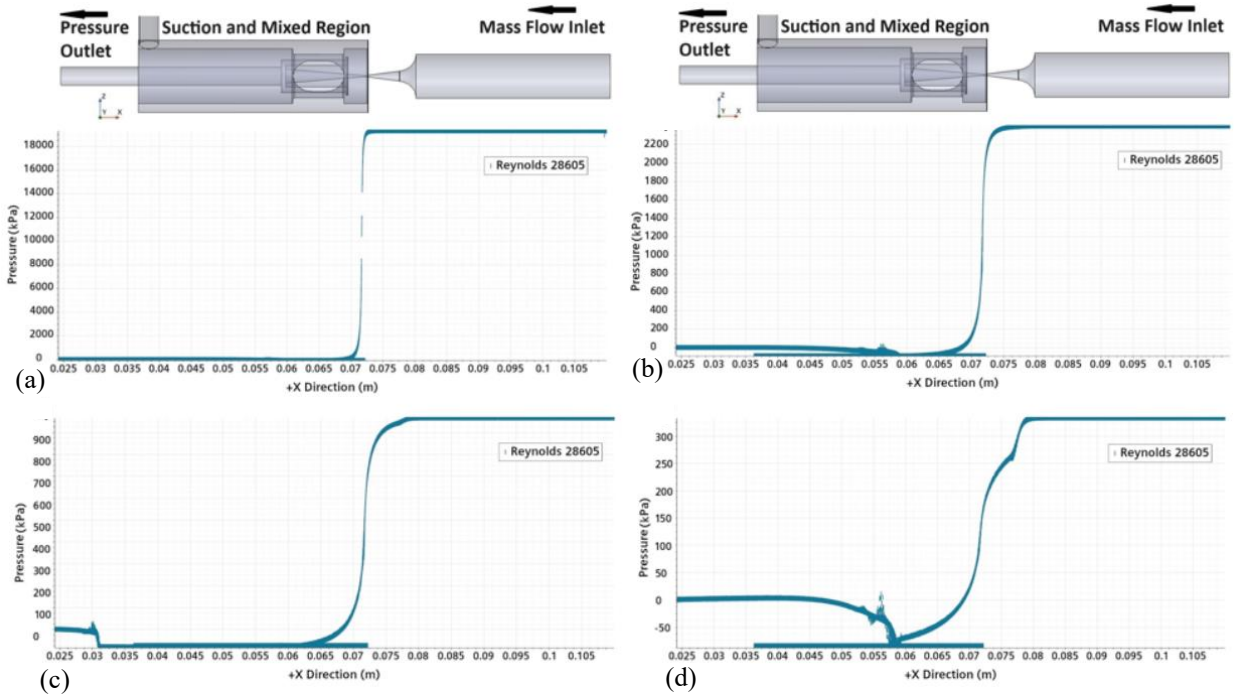

Fig 21. Pressure distributions for different throat diameters. a) Ø0.2, b) Ø0.6, c) Ø1, and d) Ø1.6 mm

described in Figs. 14 and 15. Given that the vacuum ejector keeps the wheel valve spool open by creating a vacuum, the Mach number must remain supersonic up to the pressure outlet for effective vacuum formation. Fluctuations in vacuum pressure can cause the wheel valve spool to close, preventing air from being released into the wheel.

Figure 21 shows the pressure distributions for throat diameters of 0.2, 0.6, 1, and 1.6 mm. Very high pressures are observed at the inlet for Ø0.2 mm, as shown in Fig. 21a. In Fig. 21b (Ø0.6 mm), the inlet pressure drops to approximately 2200 kPa; in Fig. 21d (Ø1.6 mm), this pressure is 300 kPa. In Fig. 21c (Ø1 mm), the pressure entering the vacuum ejector is 900 kPa, but it decreases after the constriction at the throat because of the constriction. After the constriction, the pressure becomes negative until the ejector's exit. For other diameters, the ejector does not maintain a negative pressure throughout its length. Therefore, a 1 mm throat diameter yields better results, i.e., higher vacuum levels, than other throat diameters.

6. CONCLUSION

This study investigates experimentally and numerically a vacuum ejector with a nozzle throat measuring 1.2 mm in diameter, a tool used to maintain the open state of the wheel valve in a CTIS. We validated experimental results using numerical simulations, examining vacuum values by varying the throat diameter. A theoretical model of the vacuum ejector was developed, and the mass flow rates were compared with the experimental results. The numerical studies employed a three-dimensional compressible flow model with the *k-ε* turbulence model, focusing on parameters such as throat diameter, mass flow rate, temperature, pressure, and Mach number. Below are the key finding and their implications:

- The vacuum pressure at the suction surface increases with a reduction in throat diameter and an increase in the inlet mass flow rate. However, throat diameters smaller than 1 mm lead to flow instability and choking. At throat diameters of 1 and 1.2 mm, vacuum pressures are similar at Reynolds numbers exceeding 26,800. This suggests that either diameter can be used under such conditions without significant performance loss. The optimal vacuum pressure of −98.6 kPa was achieved experimentally at Re = 34,326 and a throat diameter of 1 mm.
- Smaller throat diameters demonstrate higher vacuum pressures at lower Reynolds numbers, indicating potential for energy-efficient designs. For example, a vacuum pressure of −68.3 kPa was achieved at a Reynolds number of 20,023 with a 1 mm throat diameter, compared to −55.7 kPa with a 1.2 mm throat diameter. A comparative analysis revealed a 22.6% improvement in vacuum performance for the 1 mm throat at lower Reynolds numbers. Excessively narrow throat diameters (≤0.2 mm) resulted in complete flow choking, emphasising the need for precise geometric optimisation. Reynolds number calculations for throat diameters ≤0.5 mm consistently show deviations exceeding 15% compared to theoretical predictions, highlighting the need for precise geometrical optimisation.
- The analysis of velocity and pressure distributions reveals that the vacuum ejector achieves optimal performance when the fluid velocity is maintained at supersonic levels near the ejector exit. This ensures effective vacuum formation and minimises fluctuations that could disrupt the wheel valve

operation. The relationship between Mach number and temperature is consistent with theoretical expectations, with high velocities corresponding to significant temperature drops. For instance, at a Reynolds number of 34,326, the temperature decreased to approximately 100 K in regions of maximum velocity.

- For Reynolds numbers exceeding 26,800, both 1 and 1.2 mm throat diameters are effective. However, for optimal energy efficiency and performance, a throat diameter of 1 mm is recommended. Future research should explore the optimisation of the pressurised air input diameter in conjunction with the throat diameter to further enhance ejector performance and energy efficiency.
- The *k-ε* and *k-ω* SST turbulence models were compared with the experimental results. Numerical studies conducted using both turbulence models yielded closely aligned results for key parameters such as vacuum pressure, velocity, and temperature.

Future research in this field should focus on several key areas to improve the understanding and performance of vacuum ejectors. One crucial aspect is regarding the effects of nozzle geometry (not just throat diameter) and its impact on flow stability. Additionally, incorporating advanced turbulence models, such as LES, can provide a more accurate representation of the complex flow dynamics within these systems. Furthermore, exploring multi-phase flow conditions and their influence on vacuum ejector performance in a variety of industrial applications may offer valuable insights for optimising both design and functionality.

CONFLICT OF INTEREST

The authors declare that they have no known competing financial interests or personal relationships that could have appeared to influence the work reported in this paper.

ACKNOWLEDGMENTS

This research was supported by TÜBİTAK (The Scientific and Technological Research Council of Turkey) under Project Number 3191992. We sincerely thank TÜBİTAK for their financial support and assistance.

AUTHORS CONTRIBUTION

The contributions of each author to this work are specified according to the CRediT taxonomy as follows: **Yavuz Selim Korkmaz:** Conceptualization, Methodology, Data Curation, Writing – Original Draft, Supervision. **Ali Kibar:** Formal Analysis, Investigation, Writing – Review & Editing. **Kadri Süleyman Yiğit:** Literature Review, Writing – Review & Editing. **Ercan Ertürk:** Conceptualization, Formal Analysis. **Zafer Doğruyol:** Experimental Work, Design Studies.

REFERENCES

Akteriana, S. (2011). Improving the energy efficiency of traditional multi-stage steam-jet-ejector vacuum systems for deodorizing edible oils. *Procedia Food Science,1*,1785–1791. https://doi.org/10.1016/j.profoo.2011.09.262

Ariafar, K., Buttsworth, D., Al-Doori, G., & Malpress, R. (2015). Effect of mixing on the performance of wet steam ejectors. *Energy*, *93*, 2030–2041. https://doi.org/10.1016/j.energy.2015.10.082

Besagni, G. (2019). Ejectors on the cutting edge: The past, the present and the perspective. *Energy, 170*, 998–1003. https://doi.org/10.1016/j.energy.2018.12.214

Besagni, G., Cristiani, N., Croci, L., Guédon, G. R., & Inzoli, F. (2021). Computational fluid-dynamics modelling of supersonic ejectors: Screening of modelling approaches, comprehensive validation and assessment of ejector component efficiencies. *Applied Thermal Engineering 186*, 116431. https://doi.org/10.1016/j.applthermaleng.2020.116431Get rights and content

Cantwell, B. J. (2018). AA210A Fundamentals of Compressible Flow. Stanford University, Department of Aeronautics and Astronautics.

Chai, Y., Lin, Y., Xiao, Q., Huang, C., Ke, H., & Li, B. (2024). Numerical simulation on two-phase ejector with non-condensable gas. *Energies, 17*, 1341. https://doi.org/10.3390/en17061341

Chen, W., Shi, C., Zhang, S., Chen, H., Chong, D., & Yan, J. (2017). Theoretical analysis of ejector refrigeration system performance under overall modes. *Applied Energy, 185*, 2074–2084. https://doi.org/10.1016/j.apenergy.2016.01.103

Croquer, S., Lamberts, O., Poncet, S., Moreau, S., & Bartosiewicz, Y. (2022). Large eddy simulation of a supersonic air ejector. *Applied Thermal Engineering, 209*, 118177. https://doi.org/10.1016/j.applthermaleng.2022.118177

Dadpour, D., Lakzian, E., Gholizadeh, M., Ding, H., & Han, X. (2022). Numerical modeling of droplets injection in the secondary flow of the wet steam ejector in the refrigeration cycle. *International Journal of Refrigeration, 136*, 103–113. https://doi.org/10.1016/j.ijrefrig.2022.01.026

El-Dessouky, H., Ettouney, H., Alatiqi, I., & Al-Nuwaibit, G. (2002). Evaluation of steam jet ejectors. *Chemical Engineering and Processing: Process Intensification, 41*(6), 551–561. https://doi.org/10.1016/S0255-2701(01)00176-3

Feng, H., Yao, A., Han, Q., Zhang, H., Jia, L., & Sun, W. (2024). Effect of droplets in the primary flow on ejector performance of MED-TVC systems. *Energy, 293*, 130741. https://doi.org/10.1016/j.energy.2024.130741

Ghorbanian, S., & Nejad, S. J. (2011). Ejector modeling and examining of possibility of replacing liquid vacuum pump in vacuum production systems. *International Journal of Chemical Engineering and Applications, 2*(2), 91. https://doi.org/10.7763/IJCEA.2011.V2.82

Gullo, P., Tsamos, K. M., Hafner, A., Banasiak, K., Yunting, T. G., & Tassou, S. A. (2018). Crossing CO2 equator with the aid of multi-ejector concept: A comprehensive energy and environmental comparative study. *Energy, 164*, 236–263. https://doi.org/10.1016/j.energy.2018.08.205

Guo, Z., Deng, G., Fan, Y., & Chen, G. (2016). Performance optimization of adiabatic compressed air energy storage with ejector technology. *Applied Thermal Engineering, 94*, 193–197. https://doi.org/10.1016/j.applthermaleng.2015.10.047

Han, Y., Wang, X., Sun, H., Zhang, G., Guo, L., & Tu, J. (2019). CFD simulation on the boundary layer separation in the steam ejector and its influence on the pumping performance. *Energy, 167*, 469–483. https://doi.org/10.1016/j.energy.2018.10.195

Hemidi, A., Henry, F., Leclaire, S., Seynhaeve, J. M., & Bartosiewicz, Y. (2009). CFD analysis of a supersonic air ejector. Part II: Relation between global operation and local flow features. *Applied Thermal Engineering, 29*(14–15), 2990–2998. https://doi.org/10.1016/j.applthermaleng.2009.03.019

Hou, Y., Chen, F., Zhang, S., Chen, W., Zheng, J., Chong, D., & Yan, J. (2022). Numerical simulation study on the influence of primary nozzle deviation on the steam ejector performance. *International Journal of Thermal Sciences, 179*, 107633. https://doi.org/10.1016/j.ijthermalsci.2022.107633

Hwang, J. J., Cho, C. C., Wu, W., Chiu, C. H., Chiu, K. C., & Lin, C. H. (2015). Numerical and experimental investigation into passive hydrogen recovery scheme using vacuum ejector. *Journal of Power Sources, 275*, 539–546. https://doi.org/10.1016/j.jpowsour.2014.11.057

Kibar, A., Korkmaz, Y. S., & Yigit, K. S. (2025). Examination of flow in the monoblock directional valve: from pump to tank. *Journal of the Brazilian Society of Mechanical Sciences and Engineering, 47,* 125. https://doi.org/10.1007/s40430-025-05440-0

Koirala, R., Ve, Q. L., Zhu, B., Inthavong, K., & Date, A. (2021). A review on process and practices in operation and design modification of ejectors. *Fluids, 6*, 409. https://doi.org/10.3390/fluids6110409

Kuo, J. K., Wu, P. R., Yang, T. F., & Yan, W. M. (2023). Optimal technical analysis of vacuum ejector for passive hydrogen recovery. *International Journal of Hydrogen Energy, 48*(22), 8260–8272. https://doi.org/10.1016/j.ijhydene.2022.11.218

Li, Z., Xu, W., Liang, T., Ye, W., & Zhang, Z. (2024). Experimental and numerical studies on the performance of supersonic multi-nozzle ejector. *Appl. Therm. Eng. 242*, 122409. https://doi.org/10.1016/j.applthermaleng.2024.122409

Macia, L., Castilla, R., & Gámez, P. J. (2019). Simulation of ejector for vacuum generation. *IOP Conference Series: Materials Science and Engineering, 659*(1), 012002. https://doi.org/10.1088/1757-899X/659/1/012002

Metin, C., Gök, O., Atmaca, A. U., & Erek, A. (2019). Numerical investigation of the flow structures inside mixing section of the ejector. *Energy, 166*, 1216–1228. https://doi.org/10.1016/j.energy.2018.10.095

Mukhtar, H. K., Fadlalla, A., Ibrahim, R., & Ghani, S. (2024). Numerical investigation of the flow characteristics inside a supersonic vapor ejector. *International Journal of Thermofluids, 24*, 100912. https://doi.org/10.1016/j.ijft.2024.100912

Niu, L., & Zhang, X. (2024). Comparison of the performance enhancement of vacuum ejector by means of structure optimization and bypass methods. *Energy, 297*, 131263. http://dx.doi.org/10.2139/ssrn.4471729

Palacz, M., Haida, M., Smolka, J., Plis, M., Nowak, A. J., & Banasiak, K. (2018). A gas ejector for CO2 supercritical cycles. *Energy, 163*, 1207–1216. https://doi.org/10.1016/j.energy.2018.09.030

Ramesh, A. S., & Sekhar, S. J. (2018). Experimental and numerical investigations on the effect of suction chamber angle and nozzle exit position of a steam-jet ejector. *Energy, 164*, 1097–1113. https://doi.org/10.1016/j.energy.2018.09.010

Sadeghiseraji, J., Garcia-Vilchez, M., Castilla, R., & Raush, G. (2024). Recent advances in numerical simulation of ejector pumps for vacuum generation—A Review. *Energies, 17*(17), 4479. https://doi.org/10.3390/en17174479

Saini, M., Nur, R., Yunus, S., & Ibrahim, I. (2018). The influence of throat length and vacuum pressure on air pollutant filtration using ejector. *AIP Conference Proceedings, 1977*(1). https://doi.org/10.1063/1.5042959

Samsam-Khayani, H., Yoon, S. Y., Kim, M., & Kim, K. C. (2023). Experimental and numerical study on low-temperature supersonic ejector. *International Journal of Thermofluids, 20* (June), 100407. https://doi.org/10.1016/j.ijft.2023.100407

Siemens. (2023). *Simcenter STAR-CCM+ User Guide*. Siemens Digital Industries Software.

Sun, W., Liu, C., Zhang, H., Sun, W., Xue, H., & Jia, L. (2022). Numerical analysis of two-stage vacuum ejector performance considering the influence of phase transition and non-condensable gases. *Applied Thermal Engineering, 213*, 118730. https://doi.org/10.1016/j.applthermaleng.2022.118730

Talebiyan, M. A., Nili-Ahmadabadi, M., & Ha, M. Y. (2024). Adjoint optimization of a supersonic ejector for under-expanded, isentropic, and over-expanded

primary flow modes. *Chemical Engineering Science 292*, 119979. https://doi.org/10.1016/j.ces.2024.119979

Tang, Y., Li, Y., Liu, Z., Wu, H., & Fu, W. (2017). A novel steam ejector with auxiliary entrainment for energy conservation and performance optimization. *Energy Conversion and Management, 148*, 210–221. https://doi.org/10.1016/j.enconman.2017.05.076

Tavakoli, M., Nili-Ahmadabadi, M., Joulaei, A., and Ha, M. Y. (2023). Enhancing subsonic ejector performance by incorporating a fluidic oscillator as the primary nozzle: a numerical investigation. *International Journal of Thermofluids, 20*, 100429. https://doi.org/10.1016/j.ijft.2023.100429

Thongtip, T., & Aphornratana, S. (2017). An experimental analysis of the impact of primary nozzle geometries on the ejector performance used in R141b ejector refrigerator. *Applied Thermal Engineering, 110*, 89–101. https://doi.org/10.1016/j.applthermaleng.2016.08.100

Udroiu, C. M., Mota-Babiloni, A., Gim´enez-Prades, P., Barrag´ an-Cervera, A., & Navarro-Esbrí J. (2023). Two-stage cascade configurations based on ejectors for ultra-low temperature refrigeration with natural refrigerants. International Journal of Thermofluids, *17* 100287. https://doi.org/10.1016/j.ijft.2023.100287

Wen, C., Gong, L., Ding, H., & Yang, Y. (2020). Steam ejector performance considering phase transition for multi-effect distillation with thermal vapour compression (MED-TVC) desalination system. *Applied Energy, 279,* 115831. https://doi.org/10.1016/j.apenergy.2020.115831

Xue, H., Wang, L., Jia, L., Xie, C., & Lv, Q. (2020). Design and investigation of a two-stage vacuum ejector for MED-TVC system. *Applied Thermal Engineering, 167*, 114713. https://doi.org/10.1016/j.applthermaleng.2019.114713

Yazici, F., Karadag, M., Gokluberk, P., & Kibar, A. (2024). Examining the uniformity of flow distribution in manifolds. *Journal of Applied Fluid Mechanics, 17*(5). https://doi.org/10.47176/jafm.17.05.2302

Zaheer, Q., & Masud, J. (2017). Visualization of flow field of a liquid ejector pump using embedded LES methodology. *Journal of Visualization, 20*, 777–788. https://doi.org/10.1007/s12650-017-0429-3